

Phd Challenge : Coupled Thermo-hydraulic analysis of a 2-D Geothermal Reservoir

Due to computational limitations, I wasn't able to use refined meshes

Full technical results are available in [the associated Jupyter Notebook](#)

Clément Rey

June 19, 2025

Disclaimer: This report addresses the new version of the PhD challenge. The report about the original version of the PhD challenge is available in the `original/` folder.

1 Introduction

Enhanced Geothermal Systems (EGS) differ fundamentally from conventional geothermal systems (CGS) by artificially creating fluid pathways in hot, dry rock formations through hydraulic fracturing. This process enables heat extraction from previously inaccessible geothermal resources.

The key physical differences between EGS and CGS are summarized in Table 1. In EGS, pore pressure remains approximately atmospheric throughout the domain, increasing locally during injection, while temperature follows the geothermal gradient initially before being modified by cold injection water (MIT, 2025).

Table 1: Comparison of EGS and Conventional Geothermal Systems

Parameter	CGS	EGS
Pore Pressure	Hydrostatic	Atmospheric
Temperature	Uniform	Gradient-based

Hence, the modeling assumptions include (Mortazavi et al., 2023) :

- constant initial pressure p_0
- geothermal temperature gradient $T_0(y) = T_{surface} + Gy$, $G > 0$
- thermal equilibrium between water and rock (Local Thermal Equilibrium, LTE)
- single-phase fluid flow

2 Mathematical Formulation

2.1 Corrected Governing Equations

The coupled thermo-hydraulic evolution in porous media is described by the following equations derived from Biot's porothermoelasticity theory :

Pressure equation:

$$\frac{\partial \Delta p}{\partial t} - c_p \nabla^2 \Delta p = \lambda_{pT} \frac{\partial \Delta T}{\partial t} \quad (1)$$

Temperature equation:

$$\frac{\partial \Delta T}{\partial t} - c_T \nabla^2 \Delta T = \lambda_{Tp} \frac{\partial \Delta p}{\partial t} \quad (2)$$

where c_p , c_T are hydraulic and thermal diffusivities ($\text{m}^2 \cdot \text{s}^{-1}$) and λ_{pT} , λ_{Tp} are coupling coefficients.

The corrections made to the original equations are:

- Removal of the s^{-1} unit from the coupling coefficients.

Furthermore, **all equations are expressed in terms of ΔT and Δp** (deviations from initial values), but this does not alter their form, as the governing equations remain linear in T and p .

Domain size The domain size is set using the characteristic diffusion length $\ell = \sqrt{avg(c_p, c_T)t}$ over one year, scaled by a factor of 10. This yields a **rectangular domain of approximately $2500 \text{ m} \times 2000 \text{ m}$** .

Boundary conditions Following Gutiérrez-Oribio and Stefanou (2024), homogeneous Neumann conditions are applied for pressure on all boundaries, and for temperature on lateral boundaries. Dirichlet conditions are imposed for temperature at the top ($T = T_s$) and bottom ($T = T_0$) of the domain. Given their high Péclet number, the wells are idealized as point sources with prescribed pressure and temperature at injection, and prescribed pressure at extraction.

2.2 Dimensionless Formulation

Using characteristic scales:

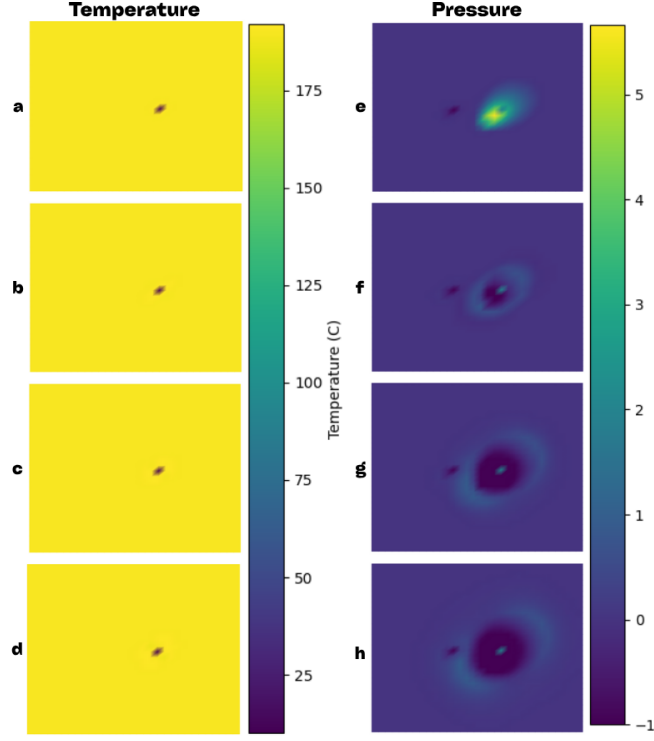


Figure 1: Temperature (a-d) and pressure (e-h) evolution after 1, 30, 180 and 365 days respectively

Lenth $L = 500 \text{ m}$: distance between wells

Time $t_c = L^2/c_p$: pressure diffusion time scale

Pressure $\Delta p_c = 3 \text{ MPa}$: Pressure difference between wells

Temperature $T_c = 180 \text{ }^\circ\text{C}$: Temperature difference between bottom and well

The dimensionless equations with point sources become:

$$\frac{\partial \hat{p}}{\partial \hat{t}} - \nabla_{\hat{x}}^2 \hat{p} = \hat{\lambda}_{pT} \frac{\partial \hat{T}}{\partial \hat{t}} + \hat{S}_{inj}^p \delta(\hat{x} - \hat{x}_{inj}) + \hat{S}_{ext}^p \delta(\hat{x} - \hat{x}_{ext}) \quad (3)$$

$$\frac{\partial \hat{T}}{\partial \hat{t}} - \hat{\kappa} \nabla_{\hat{x}}^2 \hat{T} = \hat{\lambda}_{Tp} \frac{\partial \hat{p}}{\partial \hat{t}} + \hat{S}_{inj}^T \delta(\hat{x} - \hat{x}_{inj}) \quad (4)$$

The dimensionless parameters are:

$$\begin{aligned} \hat{\kappa} &= \frac{c_T}{c_p}, \quad \hat{\lambda}_{Tp} = \lambda_{Tp} \frac{\Delta p_c}{\Delta T_c} \\ \hat{\lambda}_{pT} &= \lambda_{pT} \frac{\Delta T_c}{\Delta p_c} \end{aligned} \quad (5)$$

3 Variational Formulation

3.1 Function Spaces

We define trial spaces $V_p = \{p \in H^1(\Omega) : p|_{\partial\Omega_p^D} = p_d\}$ and $V_T = \{T \in H^1(\Omega) : T|_{\partial\Omega_T^D} = T_d\}$, with corresponding test spaces V_p^0 and V_T^0 having homogeneous boundary conditions. All Neumann boundary conditions are zero leading to vanishing surface integrals.

The weak formulation seeks $(p(t), T(t)) \in V_p \times V_T$ such that for all $(\delta p, \delta T) \in V_p^0 \times V_T^0$:

$$\begin{aligned} \int_{\Omega} \left[\delta p \frac{\partial \hat{p}}{\partial \hat{t}} + \nabla_{\hat{x}} \delta p \cdot \nabla_{\hat{x}} \hat{p} \right] d\Omega = \\ \int_{\Omega} \left[\delta p \hat{\lambda}_{pT} \frac{\partial \hat{T}}{\partial \hat{t}} \right] d\Omega \\ + \hat{S}_{inj}^p \delta p(\hat{x}_{inj}) + \hat{S}_{ext}^p \delta p(\hat{x}_{ext}) \end{aligned} \quad (6)$$

$$\begin{aligned} \int_{\Omega} \left[\delta T \frac{\partial \hat{T}}{\partial \hat{t}} + \hat{\kappa} \nabla_{\hat{x}} \delta T \cdot \nabla_{\hat{x}} \hat{T} \right] d\Omega = \\ \int_{\Omega} \left[\delta T \hat{\lambda}_{Tp} \frac{\partial \hat{p}}{\partial \hat{t}} \right] d\Omega \\ + \hat{S}_{inj}^T \delta T(\hat{x}_{inj}) \end{aligned} \quad (7)$$

3.2 Singularities caused by the point sources

The Dirac delta functions modeling point sources introduce singularities that result in unbounded gradients

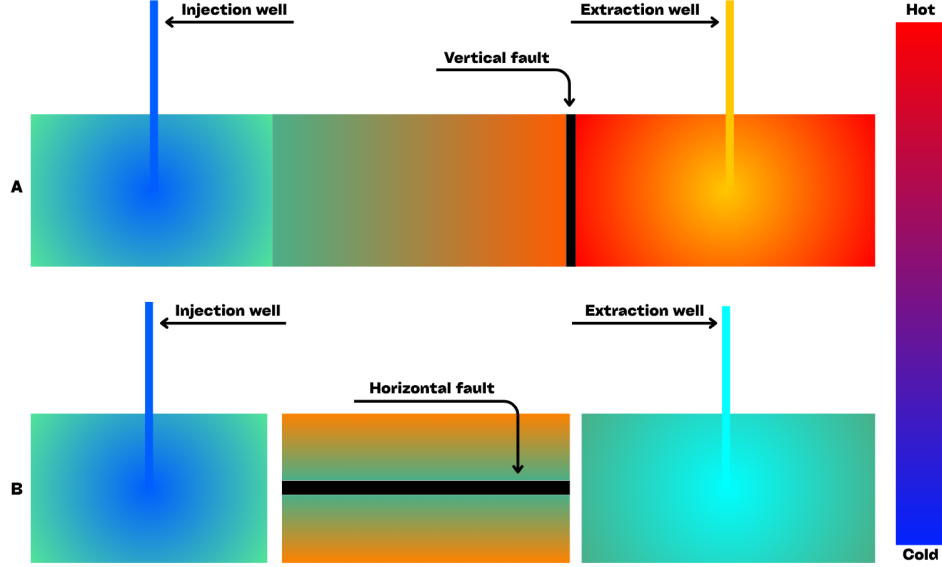


Figure 2: Extraction well : **A** warmer due to perpendicular fault, **B** colder due to aligned fault

($\nabla p, \nabla T \rightarrow \infty$), loss of solution regularity, numerical instabilities, and convergence issues. Possible solutions include **Gaussian Regularization**, which replaces the Dirac delta with a smooth approximation but is mesh-dependent, and **Asymptotic Expansion Near Source**, which uses analytical forms like $p(r, \theta) \propto \ln r$ implemented by specific elements (e.g., Barsoum-like) which is exact but complex to implement.

The **eXtended Finite Element Method** (XFEM) enriches standard finite elements with singular functions but has conditioning issues (Béchet et al., 2004), and J-integral-like regularization defines path-independent energy functionals to capture far-field behavior without directly modeling singularities but may not apply to a diffusive system.

3.3 Numerical Implementation

For time discretization, Runge-Kutta methods could have been employed. However, inspired from Scikit-fem examples, the **θ -method** with $\theta = 0.5$ is employed where spatial terms are approximated as:

$$\nabla \hat{p} \approx \theta \nabla \hat{p}^{n+1} + (1 - \theta) \nabla \hat{p}^n$$

The discretized system without point sources is:

$$\begin{bmatrix} \hat{\mathbb{M}}_p + \theta \hat{\Delta} t \hat{\mathbb{L}}_p & -\hat{\lambda}_{pT} \hat{\mathbb{M}}_p \\ -\hat{\lambda}_{Tp} \hat{\mathbb{M}}_T & \hat{\mathbb{M}}_T + \hat{\kappa} \theta \hat{\Delta} t \hat{\mathbb{L}}_T \end{bmatrix} \begin{bmatrix} \hat{p}^{n+1} \\ \hat{T}^{n+1} \end{bmatrix} = \begin{bmatrix} \hat{\mathbb{M}}_p - (1 - \theta) \hat{\Delta} t \hat{\mathbb{L}}_p & -\hat{\lambda}_{pT} \hat{\mathbb{M}}_p \\ -\hat{\lambda}_{Tp} \hat{\mathbb{M}}_T & \hat{\mathbb{M}}_T - \hat{\kappa} (1 - \theta) \hat{\Delta} t \hat{\mathbb{L}}_T \end{bmatrix} \begin{bmatrix} \hat{p}^n \\ \hat{T}^n \end{bmatrix} \quad (8)$$

where \mathbb{M} and \mathbb{L} represent mass and laplacian operators, respectively.

A Gmsh-generated mesh (Geuzaine and Remacle, 2009) is used, featuring local refinement around source points

and second-order triangular elements to enhance numerical stability. Simulations are conducted using a linear solver with a time step of 1 day, far below the CFL limit.

As mentioned in the introduction, I was not able to use the fine Gmsh mesh due to computational limitations, leading to coarse meshes. Therefore, unable to use classical regularization techniques, I used gradient capping to limit divergence near point source.

3.4 Discussion about results

The first noticeable observation is that pressures diverges on the first timestep near the extraction well before going back to acceptable values thanks to gradient capping. This behaviour may be explained by the instability caused by point sources on a very coarse mesh. Another interesting observation is that temperature barely evolves, which may be an effect of the great difference in coupling constants and the coarse mesh.

One limitation of the simulation is that the spatial resolution is not large enough, leading to very coarse results and diverging solutions. Pressure-temperature fields do not seem to stabilize after 200 days, which can be explained by small coupling coefficients and diverging solutions due to coarse meshes.

4 Fault Extension

4.1 Variational Formulation with Faults

For a fault Γ with unit normal \vec{n} and jump operator $\llbracket u \rrbracket = u^+ - u^-$, integration by parts introduces interfacial terms:

$$\begin{aligned}
& \int_{\Omega} \left[\delta p \frac{\partial \hat{p}}{\partial \hat{t}} + \nabla_{\hat{x}} \delta p \cdot \nabla_{\hat{x}} \hat{p} \right] d\Omega = \\
& \int_{\Omega} \left[\delta p \hat{\lambda}_{pT} \frac{\partial \hat{T}}{\partial \hat{t}} \right] d\Omega + \int_{\Gamma} \delta p (\hat{\alpha}_p [[\hat{p}]]) d\Gamma \quad (9) \\
& \int_{\Omega} \left[\delta T \frac{\partial \hat{T}}{\partial \hat{t}} + \hat{\kappa} \nabla_{\hat{x}} \delta T \cdot \nabla_{\hat{x}} \hat{T} \right] d\Omega \\
& = \int_{\Omega} \left[\delta T \hat{\lambda}_{Tp} \frac{\partial \hat{p}}{\partial \hat{t}} \right] d\Omega + \int_{\Gamma} \delta T (\hat{\alpha}_T [[\hat{T}]]) d\Gamma \quad (10)
\end{aligned}$$

where $\hat{\alpha}_p$ and $\hat{\alpha}_T$ are interfacial coupling parameters.

4.2 Numerical Methods for Fault Modeling

Given the fault is large, it requires an explicit approach. Among them, I would choose :

eXtended Finite Element Method (XFEM): Allows representation of discontinuities without mesh conformity through enrichment functions. Handles strong discontinuities in displacement and weak discontinuities in pressure/temperature fields (Yan et al., 2022; Mor-tazavi et al., 2023).

Finite-Discrete Element Method (FDEM): Combines FEM and DEM benefits, particularly suited for dynamic fracture propagation in EGS (Yan et al., 2022).

Spectral Boundary Element Method (S-BEM): Only meshes the fault and uses FFT to accelerate computations of planar geometries. The exact solution is known through the boundary integral equation, and the computation is of complexity $\mathcal{O}(N \ln N)$ (Bagur, 2024).

For modeling oblique faults, I would implement XFEM for its mesh independence, FDEM if fault propagation is critical and S-BEM if computational efficiency is critical.

4.3 Physical Effects

Oblique normal faults significantly impact system performance:

Pressure drawdown: High-permeability faults (up to 10^5 times matrix permeability) create preferential flow paths. Alignment with injection-production diagonal accelerates pressure drop, while perpendicular orientation acts as a barrier (Lv et al., 2022; Okoroafor et al., 2022).

Thermal breakthrough and Heat extraction performance: Fault-injection-production alignment creates short-circuits, leading to premature thermal breakthrough and reduced heat extraction efficiency as seen in figure 2. Perpendicular faults delay breakthrough and lead to a better heated fluid as seen in figure 2 (Lv et al., 2022; Okoroafor et al., 2022).

5 Control Strategy

5.1 System Definition

The control system is defined with:

- **Input:** Injection flux q_i (represented by S_{inj}^p)
- **Outputs:** Extraction temperature T_e , inj/ext pressures p_e, p_i , extraction flux q_e , seismicity rate SR
- **External inputs:** Power demand $D(t)$, injection temperature T_i

Power output is approximated as $W = \rho c_p (T_e - T_{min})$ and linearized around the operating point (q_e^*, T_e^*) because demand is smoothed out with a storage device (Daniilidis et al., 2017).

5.2 Constraints and Objectives

Hard constraints (must always be met):

$$T_e > T_{min} + \delta T = r_T \quad (11)$$

$$\Delta p = p_e - p_i > \Delta p_{min} + \delta \Delta p = r_p \quad (12)$$

with $\delta \Delta p$ and δT safety margins.

Soft constraints: Minimize tracking errors for power demand, seismicity rate, and control variations.

5.3 Control Architecture

Following (Daniilidis et al., 2017; Gutiérrez-Oribio and Stefanou, 2024; Gutiérrez-Oribio et al., 2024), I propose a hierarchical control structure shown in figure 3:

Model Predictive Controller (MPC): Optimizes injection flux over prediction horizon N_p using a Reduced-Order Model (ROM):

$$\begin{aligned}
\min_{q_i, k:k+N_p} J = & \sum_{j=0}^{N_p} [\alpha_w e_{W,k+j} + \alpha_T P_{T,k+j} + \alpha_p P_{p,k+j} \\
& + \alpha_{SR} e_{SR,k+j} + \alpha_q e_{q,k+j}] \quad (13)
\end{aligned}$$

where P_T and P_p are penalty functions for hard constraints, e terms represent tracking errors and the constants α are the gains of the MPC.

The MPC may benefit from an **adjoint problem** which predicts well the PDE system.

Adaptive Learning Layer: A Deep Deterministic Policy Gradient (DDPG) agent periodically adjusts MPC gains to maintain long-term performance and constraint satisfaction despite model uncertainties (Gutiérrez-Oribio et al., 2024).

References

L. Bagur. Modeling fluid injection effects in dynamic fault rupture using fast boundary element methods. Technical report, Structural Mechanics, Institut Polytechnique de Paris, 2024.

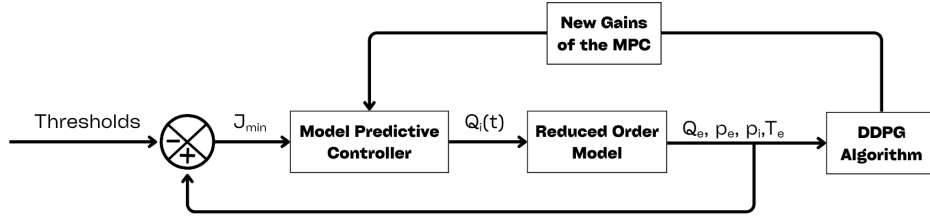


Figure 3: Schematic representation of the control loop for controlling the geothermal system. Q_i is the input pressure flux, Q_e the output pressure flux, p_i and p_e respectively the input and output pressures, T_e the output temperature and J_{min} the minimizer for the MPC.

- E. Béchet, H. Minnebo, N. Moes, and B. Burgardt. Convergence and conditioning issues with x-fem in fracture mechanics. In *WCCM VI in conjunction with AP-COM'04*, 2004.
- A. Daniilidis, T. Scholten, J. Hooghiem, C. De Persis, and R. Herber. Geochemical implications of production and storage control by coupling a direct-use geothermal system with heat networks. *Applied Energy*, 206:81–94, 2017.
- C. Geuzaine and J.-F. Remacle. Gmsh: A 3-d finite element mesh generator with built-in pre-and post-processing facilities. *International journal for numerical methods in engineering*, 79(11):1309–1331, 2009.
- D. Gutiérrez-Oribio and I. Stefanou. Insights of using control theory for minimizing induced seismicity in underground reservoirs. *Geomechanics for Energy and the Environment*, 2024.
- D. Gutiérrez-Oribio, A. Stathas, and I. Stefanou. Ai-driven approach for sustainable extraction of earth’s subsurface renewable energy while minimizing seismic activity. *International Journal for Numerical and Analytical Methods in Geomechanics*, 2024.
- Y. Lv, C. Yuan, Q. Gan, H. Li, and X. Zhu. Analysis of heat transfer based on complex embedded discrete fracture network (edfn) for field-scale egs. *Geothermics*, 105:102538, 2022.
- MIT. Geothermal power plant - mit technology roadmapping. https://roadmaps.mit.edu/index.php/Geothermal_Power_Plant, 2025. Accessed June 6, 2025.
- S.M.S. Mortazavi, O. Rezaie Beydokhti, and A.R. Khoei. Modeling enhanced geothermal systems using a hybrid xfem–ecm technique. *Applied Thermal Engineering*, 230:120755, 2023.
- E.R. Okoroafor, C. Co, and R.N. Horne. Numerical investigation of the impact of fracture aperture anisotropy on egs thermal performance. *Geothermics*, 104:102460, 2022.
- C. Yan, Y. Gao, and H. Guo. A fdem based 3d discrete mixed seepage model for simulating fluid driven fracturing. *Engineering Analysis with Boundary Elements*, 140:447–467, 2022.